# Mapping Myocardial Fiber Orientation Using Echocardiography-Based Shear Wave Imaging

Wei-Ning Lee, Mathieu Pernot*, Mathieu Couade, Emmanuel Messas, Patrick Bruneval, Alain Bel, Albert A. Hagège, Mathias Fink, and Mickaël Tanter

***Abstract*—The assessment of disrupted myocardial fiber arrangement may help to understand and diagnose hypertrophic or ischemic cardiomyopathy. We hereby proposed and developed shear wave imaging (SWI), which is an echocardiography-based, noninvasive, real-time, and easy-to-use technique, to map myofiber orientation. Five *in vitro* porcine and three *in vivo* open-chest ovine hearts were studied. Known in physics, shear wave propagates faster along than across the fiber direction. SWI is a technique that can generate shear waves travelling in different directions with respect to each myocardial layer. SWI further analyzed the shear wave velocity across the entire left-ventricular (LV) myocardial thickness, ranging between 10 (diastole) and 25 mm (systole), with a resolution of 0.2 mm in the middle segment of the LV anterior wall region. The fiber angle at each myocardial layer was thus estimated by finding the maximum shear wave speed. In the *in vitro* porcine myocardium ($n = 5$), the SWI-estimated fiber angles gradually changed from $+80^\circ \pm 7^\circ$ (endocardium) to $+30^\circ \pm 13^\circ$ (midwall) and $-40^\circ \pm 10^\circ$ (epicardium) with $0^\circ$ aligning with the circumference of the heart. This transmural fiber orientation was well correlated with histology findings ($r^2 = 0.91 \pm 0.02, p < 0.0001$). SWI further succeeded in mapping the transmural fiber orientation in three beating ovine hearts *in vivo*. At midsystole, the average fiber orientation exhibited $71^\circ \pm 13^\circ$ (endocardium), $27^\circ \pm 8^\circ$ (midwall), and $-26^\circ \pm 30^\circ$ (epicardium). We demonstrated the capability of SWI in mapping myocardial fiber orientation *in vitro* and *in vivo*. SWI may serve as a new tool for the noninvasive characterization of myocardial fiber structure.**

***Index Terms*—Anisotropy, echocardiography, fiber, myocardium, shear wave.**

## I. Introduction

THE heart wall is primarily composed of myofibers, which are arranged into layers and whose orientation in the left ventricle varies transmurally from approximately $-60^\circ$ near the epicardium to $+60^\circ$ near the endocardium [1], [2]. This transmural structural variation is highly associated with myocardial deformation [3]–[5], mechanical properties, and electrical activation [6]–[9]. Cardiac pathologies, such as postinfarction remodeling and hypertrophic cardiomyopathy, are typically accompanied by fibrosis and myocardial fiber disorganization. Therefore, the evaluation of myocardial fiber orientation may benefit the understanding of cardiac function along with the other aforementioned electromechanical elements and provide additional clinical diagnostic value.

Current approaches to measuring myocardial fiber orientation include histology and imaging techniques, such as optical coherent tomography [10], two-photon microtomy [11], and diffusion tensor magnetic resonance imaging (DT-MRI) [12], [13]. Nevertheless, histology requires thin-sliced myocardial specimens, involves cumbersome spatial registration and reconstruction, and cannot be performed *in vivo* despite its standing as the current gold standard. Among those available imaging methods, DT-MRI has been extensively investigated to map the myocardial fiber structure, even in the *in vivo* configuration [14]–[16], but is often limited in scanning time efficiency and compatibility with pacemakers.

Echocardiography, on the other hand, has been routinely exploited in clinical practice to examine the dynamic cardiac geometry and function thanks to its real-time feature. Since the late eighties, a tremendous amount of research work on myocardial anisotropy using medical ultrasound has primarily focused on the attenuation or backscatter effect stemming from the orientation of the ultrasound imaging probe (i.e., angle of insonification) relative to the myocardial fiber direction in a wide range of study configurations, including *in vitro* [17]–[19], in open-chest canine [20] and murine [21] hearts *in vivo*, and in explanted formalin-fixed human myocardium [22]. Nonetheless, the analysis of attenuation or backscattered signals generally depends on the ultrasound systems used and thus requires image calibration.

Alternatively, our group has proposed the use of shear waves generated by ultrasound, termed as shear wave imaging (SWI) in this study, to noninvasively characterize soft tissues, for instance, breast and liver, at ultrafast frame rates ($>5000$ frames/s(fps)) [23], [24]. It should be noted that unlike ultrasound, which is a compressional wave, shear wave velocity is highly dependent on the cellular and higher levels of tissue structural organization. In addition, such shear wave travels at a lower speed (typically 1–10 m/s) than the transmitted or backscattered ultrasound wave (on the order of 1500 m/s) in soft tissues. The feasibility of SWI in cardiovascular applications has been recently demonstrated by our group [25], [26]. Another ultrasound-based shear wave technique, shear

Manuscript received August 17, 2011; revised October 06, 2011; accepted October 06, 2011. Date of publication October 19, 2011; date of current version March 02, 2012. This study was supported by Agence Nationale de la Recherche (ANR), Société Française de Cardiologie (SFC), and Fédération Française de Cardiologie (FFC). *Asterisk indicates corresponding author*.

W.-N. Lee, M. Fink, and M. Tanter are with the Institut Langevin, ESPCI ParisTech, CNRS UMR 7587, INSERM U979, 75005 Paris, France.

*M. Pernot is with the Institut Langevin, ESPCI ParisTech, CNRS UMR 7587, INSERM U979, 75005 Paris, France.

M. Couade is with the Institut Langevin, ESPCI ParisTech, CNRS UMR 7587, INSERM U979, 75005 Paris, France, and also with the SuperSonic Imagine, 13857 Aix en Provence, France (e-mail: mathieu.pernot@espci.fr).

E. Messas, P. Bruneval, and A. A. Hagège are with the Assistance Publique-Hôpitaux de Paris, Hôpital Européen Georges Pompidou, INSERM U633, PARCC, Université Paris Descartes, 75015 Paris, France.

A. Bel is with Hopital Europeen Georges Pompidou, INSERM U633, 75015 Paris, France (e-mail: alain.bel@egp.aphp.fr).

Color versions of one or more of the figures in this paper are available online at http://ieeexplore.ieee.org.

Digital Object Identifier 10.1109/TMI.2011.2172690

wave anisotropy imaging, was proposed and evaluated by Hsu *et al.* [27] to study tissue anisotropy as a potential tool of assessing fiber organization. Their preliminary results were provided in a computational simulation scheme and a homogeneous isotropic phantom [27]. Yet, measuring and mapping the myocardial fiber orientation *in vitro* or *in vivo* using shear wave techniques were not fully implemented and investigated.

In this paper, the goal is, therefore, twofold. First, we further develop and employ SWI for the noninvasive measurement and mapping of the transmural fiber orientation of the heart *in vitro* and validate SWI with histology. Second, the feasibility of SWI for real-time assessment of transmural fiber orientation is investigated in normal beating hearts *in vivo*. To tackle the above-mentioned issues, we begin with the fundamental (Section II-A) of the shear wave propagation in an anisotropic medium, followed by the experimental setup and cardiac sample preparation. The basics, implementation, and analysis of SWI as well as the fiber angle estimation are then described (Section II-C). Several new technical aspects of SWI in quantifying transmural myocardial fiber angles are also detailed (Section II-C). Both *in vitro* porcine and *in vivo* ovine results together with their histological validation (Section III) and discussions (Section IV) are provided. We lastly conclude with the study findings and future perspectives on SWI in cardiac applications.

## II. Methods

### A. Basic Theory

Shear waves (in the low kilohertz range) propagate in soft tissues at a speed ranging typically between 1 and 10 m/s, depending on the elastic properties of the propagation medium. In many organs, such as breast or liver, the assumption that the propagation medium be isotropic implies that shear waves propagate at the same speed in any direction, providing a unique shear modulus that quantifies the tissue stiffness. However, due to their fiber structure, the myocardium and skeletal muscles are highly anisotropic media which induce different shear wave speeds along the propagation directions.

Well documented in cardiac physiology, myocardium mainly consists of sequential layered myofiber structures across the wall [2]. The hypothesis in this study was that the myocardium was regarded as a composite of multiple transversely-isotropic thin media [Fig. 1(a)]. Well established in wave physics, shear wave propagates faster along than across the fiber direction [28] [Fig. 1(b)]. Hence, the phenomenon that the speed of a shear wave depends on its propagation direction relative to the fiber direction [28] is the key to estimating the fiber orientation in the myocardium in our study.

Assume that a shear wave propagates in a locally transversely isotropic medium with transmurally varying myofiber orientation in the local fiber coordinates $(x_1, x_2, x_3)$ [Fig. 1(a)]. The speed of the shear wave which is polarized along $(0, 0, x_3)$ and propagates in the $x_1 - x_2$ plane [e.g., $\mathbf{n}$ in Fig. 1(a)] can be formulized as [28]

$$v(\theta) = \sqrt{\frac{\mu_{\perp} \sin^2 \theta + \mu_{//} \cos^2 \theta}{\rho}} \tag{1}$$

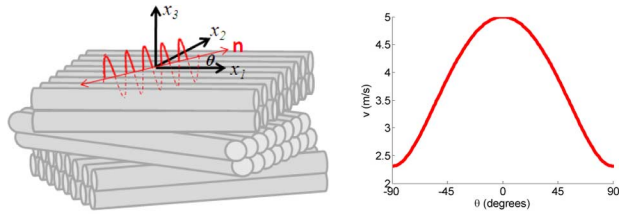


(a) (b)

Fig. 1. Illustration of the shear wave theory. (a) Simplified schematic of the myocardium, where fibers are orientated in layers with a preferred direction. For the top pile, local fiber coordinates (fiber, cross-fiber, and radial) are defined as $(x_1, x_2, x_3)$. A shear wave with its polarization in the $\overrightarrow{x_3}$ direction and propagation $(\mathbf{n})$ in the $x_1 - x_2$ plane is illustrated by the sinusoidal curve in red. $\theta$ denotes the angle between the wave propagation $(\mathbf{n})$ and fiber directions $(\overrightarrow{x_1})$. (b) Shear wave speed profile as a function of $\theta$.

where $v$ is the shear wave speed, $\theta$ is the angle between the shear wave propagation $(\mathbf{n})$ and fiber $(\overrightarrow{x_1})$ directions, $\mu_{\perp}$ and $\mu_{//}$ are elastic moduli, and $\rho$ is density. In our study, the key strategy is thereby to generate plane shear waves which propagate in a number of different directions throughout the myocardium (Section II-C1).

### B. Experimental Setup

As defined in Streeter *et al.* [2], the fibers aligned with the circumference of the left ventricle were denoted with an angle of 0°. Viewed from the anterior wall of the left ventricle, fibers that rotate clockwisely from the circumferential to the longitudinal axis of the local cardiac coordinates $(x_c, x_l, x_r)$ were assigned as negative angle values [Fig. 2(b)]; on the contrary, fibers that rotate counterclockwisely were assigned as positive angle values [Fig. 2(b)]. This denotation was adapted throughout our study.

*1) In Vitro Porcine Heart:* Five excised porcine hearts were studied and firstly embedded in a gelatin phantom to secure their position during the experimental procedure. A marker whose orientation matched the local cardiac circumferential $(\overrightarrow{x_c})$ and longitudinal $(\overrightarrow{x_l})$ axes was labeled on the epicardial surface of the target region in the left ventricle (i.e., the middle segment of the left-ventricular anterior wall) [Fig. 2(a)]. Note that the longitudinal axis was defined based on the axis that passed through the aortic root and the apex. The center of the linear array probe (Section II-C2) was coaxial with the radial direction, orthogonal to both $\overrightarrow{x_c}$ and $\overrightarrow{x_l}$, in the predefined local cardiac coordinates such that the probe rotated about the radial axis [Fig. 2(b)].

*2) In Vivo Ovine Heart:* Three sheep, weighing $49 \pm 5$ kg, were anesthetized with thiopentothal (0.5 mL/kg), intubated, ventilated at 15 mL/kg with 2% isoflurane, and given glycopyrrolate (0.4 mg intravenous) and vancomycin (0.5 g intravenous). Sterile lateral thoracotomy was performed. Vital signs, including heart rate, oxygen saturation, and arterial blood pressure, were monitored. The anterior wall at the middle left-ventricular level was selected as the region of interest (ROI). The animal procedure was approved prior to use by the Institutional Animal Care and Use Committee of l'Hôpital Européen Georges Pompidou (PARCC) according to the European Commission guiding principles (2010/63/EU).

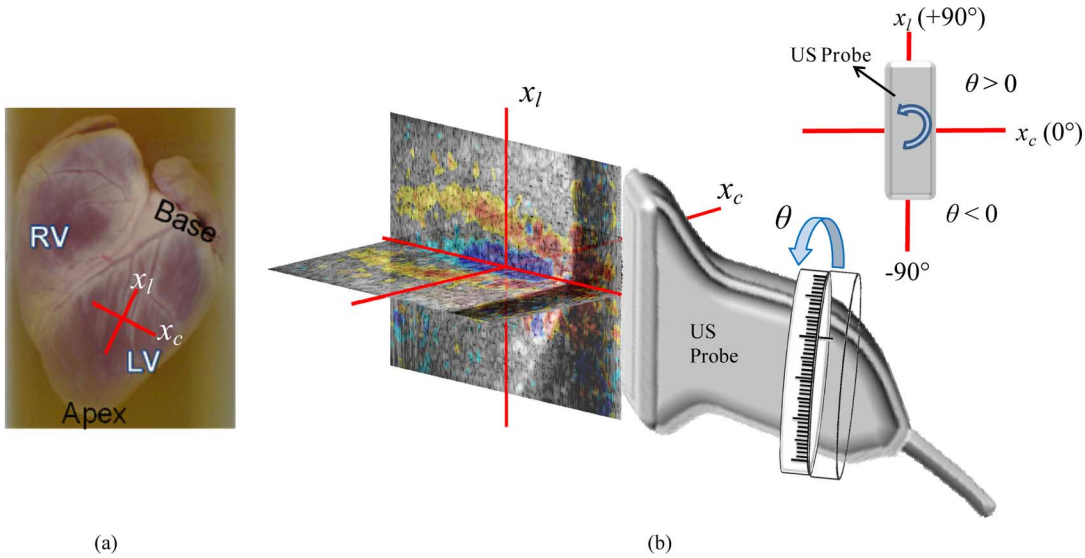


(a) (b)

Fig. 2. Myocardial sample preparation and the probe setup. (a) Excised porcine heart embedded in a gelatin phantom. The local circumferential-longitudinal coordinates, $(x_c, x_l)$, were defined by the marker in red. (b) Rotation of the ultrasound probe was realized by mounting it on a customized rotation device. The ultrasound (US) probe was initially aligned with the longitudinal direction, which was defined as $-90^\circ$ and then rotated counterclockwise by $\theta$ degrees. At each probe angle $\theta$ shear wave images were acquired.

### C. Shear Wave Imaging (SWI) [23]

*1) Principles:* Shear Wave Imaging is comprised of two major features: the generation of plane shear waves and the acquisition of the shear wave events at an ultrafast frame rate ($> 8000$ fps). The radiation force of a focused ultrasound beam from a conventional ultrasound array probe induces shear vibrations (or displacements) in the tissue and thus generates travelling shear waves. The propagation of the shear waves, whose speed typically ranges between 1 and 10 m/s, is then captured and imaged with the same array probe at ultrafast frame rate for further data analysis (Section II-C2). The polarization of the shear wave generated was in the beam (i.e., axial) direction in all cases studied in this paper. In other words, only one polarization of shear wave was exploited.

Plane shear waves were generated in a supersonic mode, where the shear source was successively generated using the acoustic radiation force at three different push depths, spaced at 5 mm, inside the myocardium along the axial direction.

Shear wave imaging achieves such ultrafast frame rates by transmitting acoustic plane waves while suffering from low echocardiographic signal-to-noise ratio (SNR) and thus degrading the tracking accuracy of the generated shear waves. Therefore, we further implemented the coherent plane-wave compounding technique [29] to improve the echocardiographic image quality. In this study, shear waves were imaged by alternately steering ultrasonic plane waves at three different angles $(-2^\circ, 0^\circ, 2^\circ)$. Coherent-compounded images of the shear waves were formed by averaging three consecutive ultrasonic plane wave images. This moving-average procedure not only improved the image SNR but also preserved the initial ultrafast frame rate.

*2) Data Acquisition:* A programmable prototype ultrasound system equipped with a conventional linear array probe (center frequency $= 8$ MHz, pitch $= 0.2$ mm, fractional bandwidth $= 90\%$) was utilized. Each pushing beam duration was 120 $\mu$s. The ultrasound probe, attached to a customized rotation device, was firstly aligned with the longitudinal axis of the ROI [Fig. 2(a)] and thereafter rotated counterclockwisely from - 90° to 90° at 5° increments [Fig. 2(b)]. In the *in vivo* ovine cardiac model, Shear Wave Imaging was performed at multiple equally sampled phases in one cardiac cycle, and the total acquisition time of each shear wave event was less than 10 ms. The electrocardiogram (ECG) was recorded at a sampling rate of 4800 Hz in synchrony with the shear wave data acquisition.

Retrospective ECG-gating was performed to synchronize the cardiac cycles acquired at all the probe angles. Shear wave images at multiple cardiac phases in one cardiac cycle for each probe angle were therefore gated in sequence from early systole to late diastole. The mid-systolic phase and its corresponding shear wave data were then selected at each probe angle for subsequent shear wave analysis.

*3) Shear Wave Tracking and Speed Estimation:* Shear wave amplitude (i.e., tissue velocity) was estimated using a standard speckle tracking method. Shear waves could be easily visualized [Fig. 3(a)] and analyzed from the sequential 2-D tissue velocity maps in a depth-by-depth fashion [indicated by the double-headed arrow in Fig. 3(a)], from epicardium toward endocardium. For each shear wave event, the shear wave tracking procedure could be summarized in the following steps. First, at each depth of interest (1–1.5 mm), a spatio-temporal (i.e., travel distance versus time) imaging of the shear wave propagation [Fig. 3(b)] was obtained from the tissue velocity maps [Fig. 3(a)]. Second, the shear wave propagation distance was estimated by tracking the wave profile in both propagation direction (i.e., lateral direction in medical ultrasound imaging, indicated by the double-headed arrow) and time domain [Fig. 3(b)]. This tracking was based on the normalized cross-correlation function

$$\rho(j) = \frac{\sum_{i=1}^{M} \left(A_i - \overline{A}\right)\left(B_{i+j} - \overline{B}\right)}{\sqrt{\sum_{i=1}^{M} \left(A_i - \overline{A}\right)^2 \sum_{i=1}^{M} \left(B_{i+j} - \overline{B}\right)^2}} \quad 0 \le j \le N - M \tag{2}$$

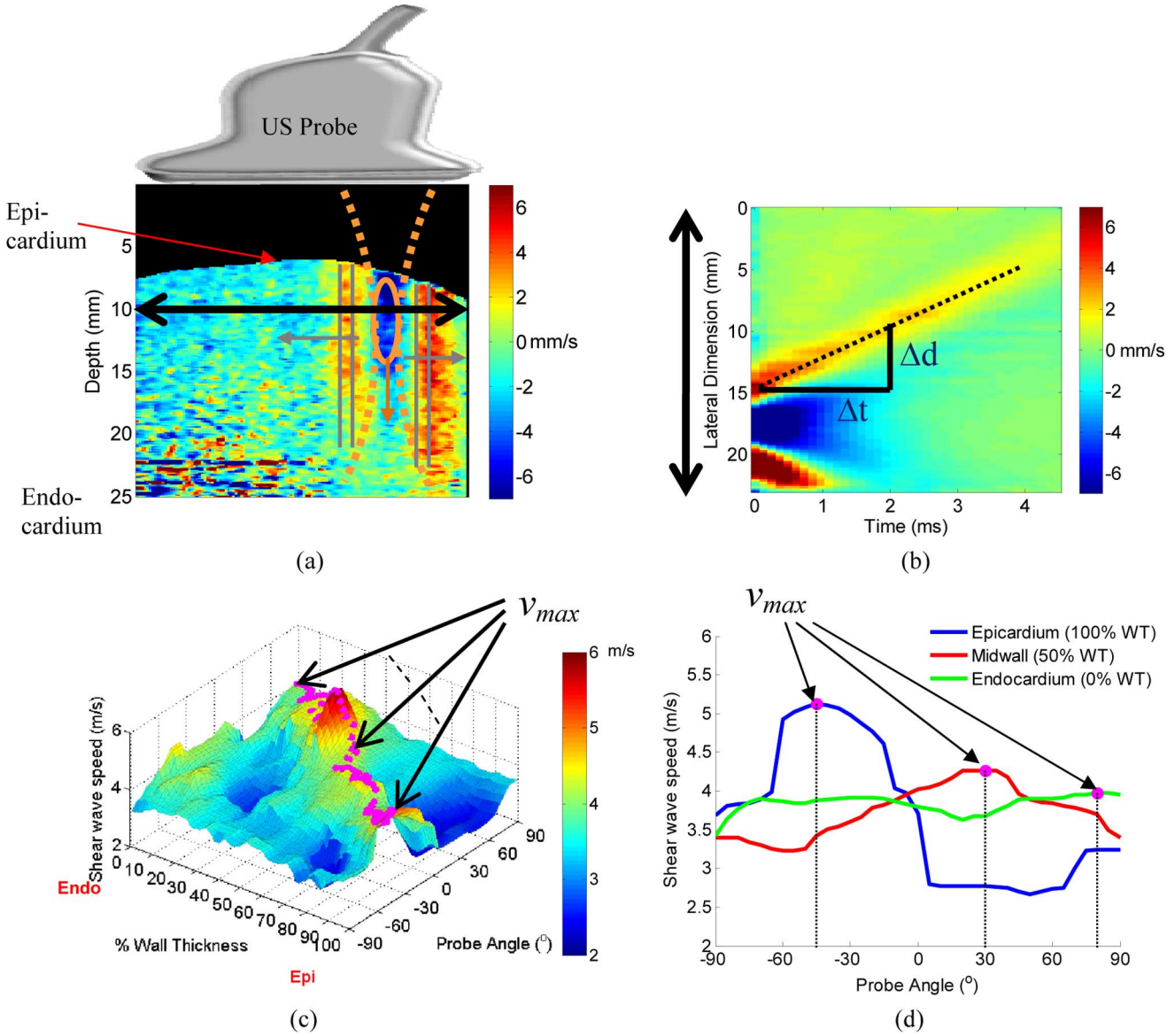


Fig. 3. Example of both the shear wave imaging and the fiber angle estimation strategies. (a) Shear wave imaging of the mid-anterior wall region in a porcine left ventricle at one probe angle. Shear wave (represented by gray solid lines and gray arrows) was induced by the radiation force of a focused ultrasound beam (denoted by orange dotted curves) with a focal zone (indicated by the orange solid ellipse). (b) Spatio-temporal (travel distance versus time) imaging of the shear wave propagation at a depth of interest indicated by the double-headed arrow in (a). The black dotted line denoted the tracked shear wave propagation path, and its slope ($\Delta d/\Delta t$) corresponded to the wave speed. (c) The surface plot of the shear wave speed across the myocardial wall [from epicardium (Epi, 100% wall thickness) to endocardium (Endo, 0% wall thickness)] for all the probe angles ($-90^\circ$ to $90^\circ$) performed. The wave speed was also presented in color as indicated by the color bar. (d) Paradigm extracted from (c), where the shear wave speed profiles are plotted as a function of probe angles at three distinct depths: epicardium, midwall, and endocardium. Maximum speed [$v_{\max}$ and filled circles in magenta color in (c) and (d)] and its associated probe angle were found to determine the corresponding fiber angle at each depth of interest. WT denotes wall thickness.

where $A$ of length $M$ was the reference wave profile at $t = 0$, $B$ of length $N$ was the comparison wave profile at $t = T$, and $N > M$. The maximum value of (2) was then found and denoted as $\rho_p$

$$\rho_p = \rho(j = p) = \max(\rho(j)). \tag{3}$$

Cosine interpolation was further applied to improve the precision in finding the true maximum cross-correlated value [30].

The shear wave group velocity was then obtained by computing the slope of the travel distance ($X_{\text{peak}}$), obtained from the cosine interpolation, to the propagation time (T)

$$v(z, x, \theta) = \frac{X_{\text{peak}}}{T} \tag{4}$$

where $v$ was the shear wave group velocity as a function of myocardial depth ($z$), lateral position ($x$), and probe angle ($\theta$). Third, the shear wave speed was therefore estimated across the entire myocardial wall at each probe angle. The shear wave speed as a function of both myocardial wall thickness and the probe angle was mapped, as shown in Fig. 3(c). Note that the myocardial wall was manually traced, and the papillary muscle, if presented in the imaging zone, was excluded for endocardial boundary extraction. The total time of computing shear wave amplitude and propagation speed for each probe angle was approximately 15 s.

In the *in vivo* configuration, the overall apparent tissue velocity was a fusion of physiologic myocardial velocity (contraction or relaxation) and particle velocity induced by the shear

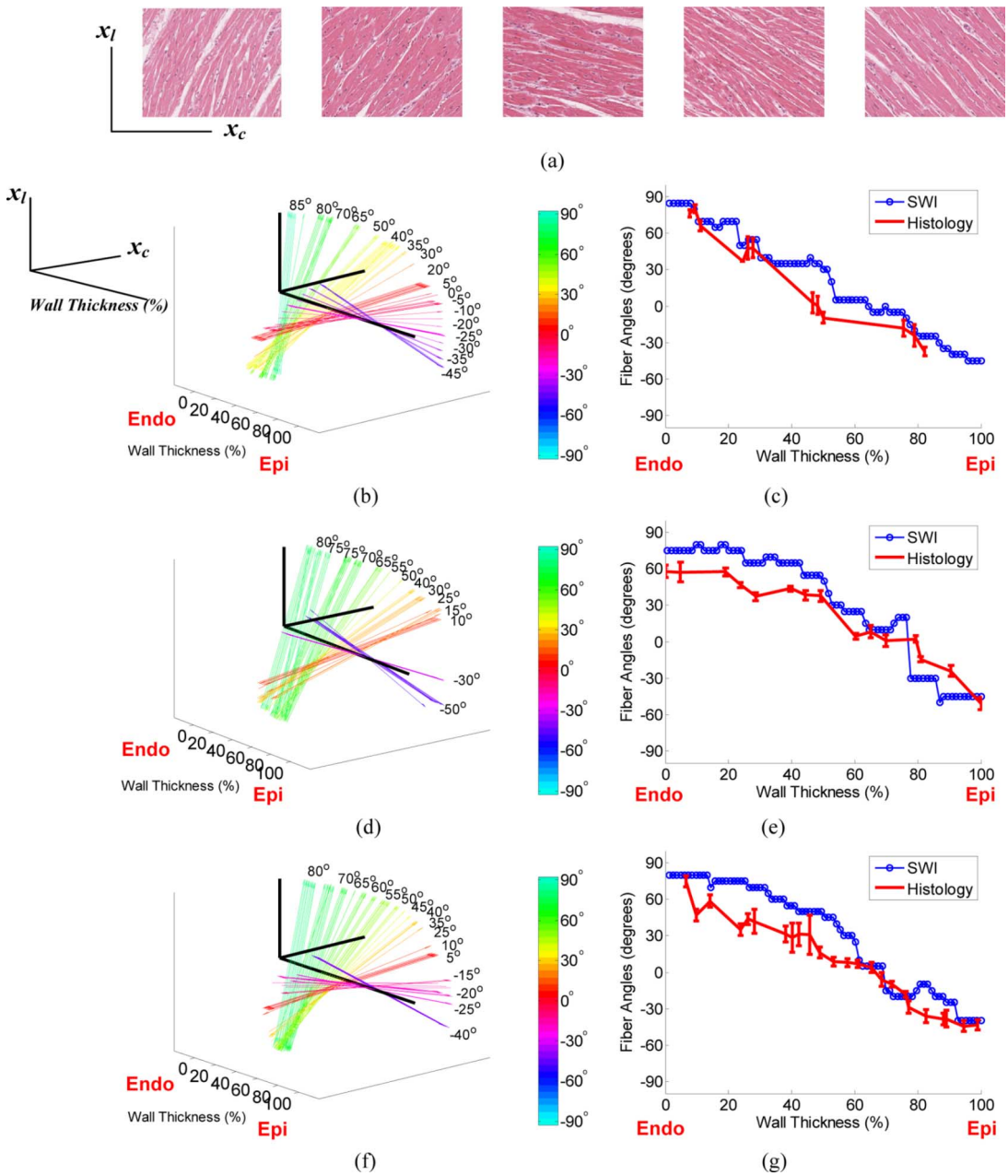


Fig. 4. The comparison of the fiber orientation between histology (H&E stain) measurement and SWI estimation in the mid-anterior wall region of the porcine left ventricle. (a) Five histology slides ($20\times$) of the same myocardial specimen shown in Fig. 2, depicting the fiber structure in the subendocardial (left) toward that in the subepicardial (right) circumferential-longitudinal slices. Images (b) and (c) are, respectively, the SWI fiber orientation plot and the comparison of transmural fiber angles between SWI and histology measurements from the same sample shown in (a). Images (d) and (f) are the fiber orientation graphs from two other different porcine specimens. Images (e) and (g) are the plots that compare SWI and histology findings from the specimens (d) and (f), respectively. 0% and 100% wall thicknesses represent the endocardium and the epicardium, respectively. $x_c$ and $x_l$ denote the circumferential and longitudinal directions, respectively. The colorbar displays the fiber angles ranging between $-90^\circ$ and $90^\circ$.

source generated using SWI. Consequently, the SWI-generated shear wave needed to be segregated from the physiologic myocardial velocity before the shear wave speed estimation (Section III-B).

*4) Myocardial Fiber Angle Estimation:* Fig. 3(c) shows the angle dependence of the shear wave speed across the myocardial wall. Recall that maximum shear wave speed occurs when the shear wave propagates along the fibers (Section II-A) (Fig. 1). At each depth, consequently, we searched for maximum shear wave speed [$v_{\max}$ in Fig. 3(c) and (d)], and the probe angle which exhibited the maximum speed was defined to be the fiber angle [$\tilde{\theta}(z)$ in (5)] [Fig. 3(c) and (d)] given that the probe angles of $0^\circ$ and $90^\circ$ were initially aligned with the circumferential $(0^\circ)$ and longitudinal $(90^\circ)$ axes, respectively, in the local cardiac coordinates (Fig. 2) prior to the examination

$$\tilde{\theta}(z) = \underset{\theta\in[-90^\circ,90^\circ]}{\operatorname{argmax}} \; v(z, x = \text{central lateral position}, \theta). \tag{5}$$

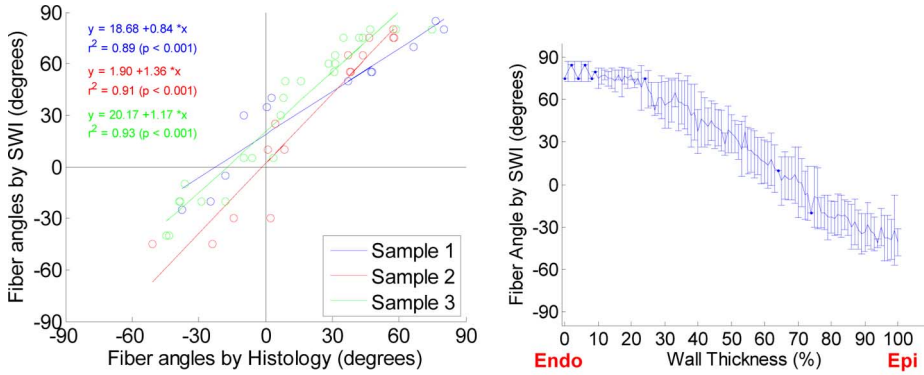


Fig. 5. Fiber angle statistics from *in vitro* porcine myocardium. (a) Correlation plot, showing the relationship of the transmural fiber angles between SWI and histology findings in three different porcine myocardial specimens. (b) Average transmural fiber angles estimated by SWI from all myocardial samples ($N = 5$) studied. 0% and 100% wall thicknesses represent the endocardium and the epicardium, respectively.

Fig. 3(d) shows an example of the shear wave speed profile as a function of the probe angle at three distinct wall depths: epicardium, midwall, and endocardium. At each depth of interest, the probe angle at which maximum shear wave speed occurred [$v_{\max}$ in Fig. 3(c) and (d)] was identified as the fiber angle. Only three wall depths (100%, 50%, and 0% wall thicknesses) were selectively shown in Fig. 3(d) in order to illustrate the fiber angle estimation strategy. Not shown in Fig. 3(d), global maximum shear wave speed (5.97 m/s) in fact occurred at 40% wall thickness [Fig. 3(c)] in this porcine myocardial sample. In other porcine samples studied, global maximum shear wave speed occurred in regions different from 40% wall thickness. The discrepancy in the wall depth where the global maximum shear wave speed exhibited may be attributed to the different stiffness from one myocardial sample to another. In this study, despite the fact that global maximum shear wave speed may have occurred at different myocardial wall depths in different specimens, the contrast in local shear wave speeds among different propagation directions at each target wall depth was the key factor in resolving the fiber angle.

### D. Histology

Guided by the epicardial marker, each myocardial region examined by SWI was dissected from the intact heart into a rectangular block ($15 \times 20 \times 25$ mm$^3$). A basal-septal (i.e., upper-left viewed from the anterior side of the myocardial block) corner cut was then performed, sliced sequentially parallel to the epicardium into circumferential-longitudinal slices with a thickness of 2 mm, and then fixed in the 10% formalin solution. Each myocardial slice was then individually embedded in paraffin and serially sectioned at 5 $\mu$m of thickness.

Each paraffin block was completely cut in consecutive sections, each of which was distant of 100 $\mu$m of the adjacent ones. All the sections were stained with hematoxylin and eosin (H&E) and scanned using optical microscopy (Tribvn, Chatillon, France). The scanned histological slides were analyzed and reconstructed based on the basal-septal corner cut to evaluate the fiber orientation. Five representative histology slices from the porcine myocardial example shown in Fig. 3 was provided in Fig. 4(a), where from the left to the right are the histological images taken from the subendocardial to subepicardial regions. Fiber angles in all the histological images studied were computed using the Hough transform [31].

## III. Results

### A. In Vitro Porcine Heart

Fig. 4(b) illustrates the SWI-estimated transmural fiber orientation in the same porcine myocardial specimen shown in Fig. 3 and Fig. 4(a). The fiber angles ranged from 85° at the endocardium (0% wall thickness) to $-45°$ at the epicardium (100% wall thickness). This transition from positive fiber angles (i.e., right diagonal) near the endocardium to negative fiber angles (i.e., left diagonal) near the epicardium was in good agreement with histology [Fig. 4(c)] and the literature [2]. SWI-estimated fiber orientation across the wall [Fig. 4(d) and (f)] and its corresponding histological examination [Fig. 4(e) and (g)] of two other porcine myocardial specimens are also shown.

For each of the three porcine myocardial samples, very good correlation was found between the SWI estimates and histology measurements [Fig. 5(a)]. The average coefficient of determinant ($r^2$) from the three porcine specimens was $0.91 \pm 0.02 (p < 0.0001)$.

The three porcine myocardial samples which were further performed with histology were chosen randomly out of the five specimens studied to ease the labor-intensive histological procedure and the postanalysis. On the other hand, the average fiber orientation from all five porcine myocardial specimens utilized [Fig. 5(b)] were computed and confirmed the transmural variation of the myocardial fiber angles and the reproducibility of the SWI technique on the evaluation of myocardial anisotropy. The average fiber angles ranged from $+80° \pm 7°$ at the endocardium to $+30° \pm 13°$ at the midwall and $-40° \pm 10°$ (epicardium). The myocardial fibers approximately spanned over 120° [Fig. 5(b)].

### B. In Vivo Ovine Heart

Retrospective ECG-gating was performed in the *in vivo* ovine heart configuration to synchronize the cardiac cycles among all the probe angles. Fig. 6 shows an example of such an ECG-gating procedure. In this ovine case, 17 shear wave events were performed at equally-spaced cardiac phases in one cardiac cycle for each probe angle. In each event, the overall apparent tissue

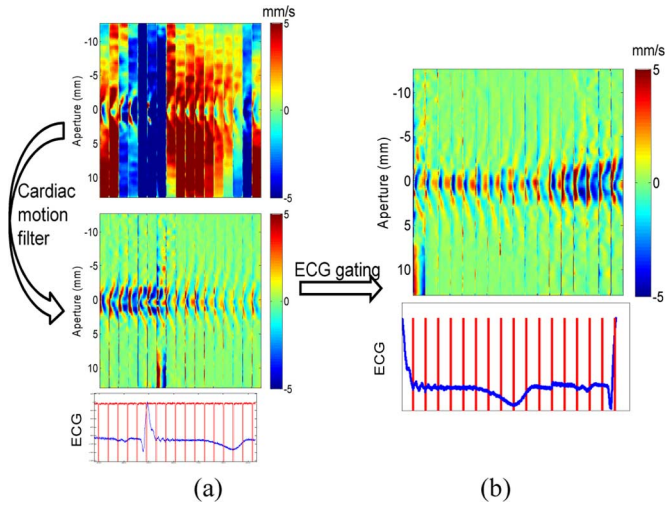


Fig. 6. Retrospective ECG-gating procedure in the anterior subepicardial wall region in one sheep *in vivo* at the probe angle of 0°. (a) Spatio-temporal imaging of the shear wave propagation before and after the removal of physiologic cardiac motion, at multiple phases in one cardiac cycle. (b) Corresponding ECG-gated, cardiac-motion-filtered spatio-temporal imaging.

velocity was a fusion of physiologic myocardial velocity (contraction or relaxation) and particle velocity induced by the shear source generated by shear wave imaging (SWI). The SWI-generated shear wave therefore needed to be segregated using a standard high-pass filter to remove the physiologic myocardial velocity, as shown in Fig. 6(a). This high-pass filter was performed in the simplest scenario where the dc component was removed from the original signals. In the *in vivo* configuration, physiologic cardiac motion was nearly steady within 2.3 ms, which was the total acquisition duration of each shear wave event. Consequently, such a steady motion was filtered out by removing the dc component of the mixed velocity data in a sample-by-sample fashion with a temporal window of 2.3 ms. Rearrangement of the cardiac phases at which shear wave events occurred was thereafter performed [Fig. 6(b)]. The end diastole (i.e., R wave of the ECG) was selected as the reference cardiac phase. Shear wave images at multiple cardiac phases in one cardiac cycle for each probe angle were therefore gated in sequence from early systole to late diastole [Fig. 6(b)]. In this pilot *in vivo* study, only the midsystolic phase was presented since it was the phase which was the compromise of large contraction rate and high shear wave speed in the ovine hearts examined.

Both transmural shear wave distribution as a function of the probe angle [Fig. 7(a)] and the corresponding fiber orientation [Fig. 7(b)] at a midsystolic phase [ECG shown in Fig. 7(a)] in the middle segment of the anterior wall region of one beating ovine heart were shown. Gradual changes of the fiber angles across the wall, ranging from 70° at the endocardium (0% wall thickness) to $-15°$ at the epicardium (100% wall thickness) were observed. Fig. 7(c) shows the average fiber orientation of the middle segment of the anterior wall region in all three *in vivo* ovine hearts at midsystole, where transmural fiber orientation estimated by SWI exhibited $71° \pm 13°$ (subendocardium), $27° \pm 8°$ (midwall), and $-26° \pm 30°$ (subepicardium). Note that the entire myocardial thickness was equally divided into 10 regions, and the mean and standard deviation of the fiber angles in each region were computed.

## IV. Discussion

All the *in vitro* porcine ($N = 5$; Figs. 4 and 5) and *in vivo* ovine ($N = 3$; Fig. 7) myocardial specimens, in the anterior wall region at the mid-left-ventricular level, showed myofibers rotating counterclockwisely from the left diagonal (negative angles) near the epicardium to the right diagonal (positive angles) near the endocardium. This transmural change of fiber angles was consistent with the literature [1], [2], [32].

In the *in vitro* examinations, the transmural fiber angles estimated using SWI followed a similar trend to those measured from histology [Fig. 4(b)–(g)]. Although there existed angle differences due to different spatial resolutions (i.e., circumferential-longitudinal slice thickness) and challenging co-registration between SWI and histology, an average coefficient of determinant of 0.91 indicates that SWI-estimated fiber angles exhibited a transmural fiber variation which was comparable to the histology finding [Fig. 5(a)]. In addition, we observed that the circumferential fibers ($\text{fiber angle} = 0°$) lay in the 60%–70% wall thickness in porcine left ventricles (Fig. 4).

An example of the fiber structure in an ovine heart at the midsystolic phase *in vivo* [Fig. 7(b)] demonstrated, for the first time, both the transmural variation of the fiber angles and the capability of SWI in quantifying myocardial fiber orientation in a beating heart. The average fiber angles estimated by SWI in three *in vivo* ovine hearts at midsystole [Fig. 7(c)] not only exhibited the gradual change in the transmural fiber orientation but also testified the feasibility of SWI in the assessment of myocardial fiber orientation in an *in vivo* configuration.

The midsystolic phase was of the main interest in this study since it was a phase with active contraction, associated with the pronounced alteration of myocardial mechanical properties (i.e., stiffness) in major myocardial diseases, such as ischemia caused by the stenosed coronary artery. It was also the phase where highest shear wave speed was found in the ovine hearts studied. Evidently, the fiber angle map at only one time point cannot be extrapolated to explain what occurs in the rest of the cycle. Examining whether and how the transmural fiber orientation varies during the cardiac cycle is absolutely one of the ultimate goals. The presented *in vivo* findings and ultrafast data acquisition (i.e., ultra high frame rates ($> 8000$ fps)) in SWI may warrant the employment of SWI for myocardial fiber imaging over the entire cardiac cycle. The dynamics of the myocardial fibers at multiple distinct cardiac phases is currently being investigated using SWI. Nonetheless, further validation of SWI with other *in vivo* measurements is deemed essential to demonstrate and verify the temporal behavior of transmural fiber orientation. Furthermore, fiber disarray has been demonstrated to correlate with the infracted and hypertrophic myocardium. Future work will also include the study of the capability of SWI in estimating and mapping fiber disorientation to aid prognosis of diseased hearts.

DT-MRI has emerged as a promising imaging technique to visualize myocardial orientation in three-dimension, but its long data acquisition duration restricts its application in the *in vivo* scenario. For example, in a DT-MRI study performed in ovine hearts [33], acquiring all reduced encoded diffusion-weighted images ($128 \times 64 \times 64$ pixels; $10 \times 10 \times 10$ cm$^3$) to be reconstructed required approximately 9.1 h. In our study, 1-D fiber

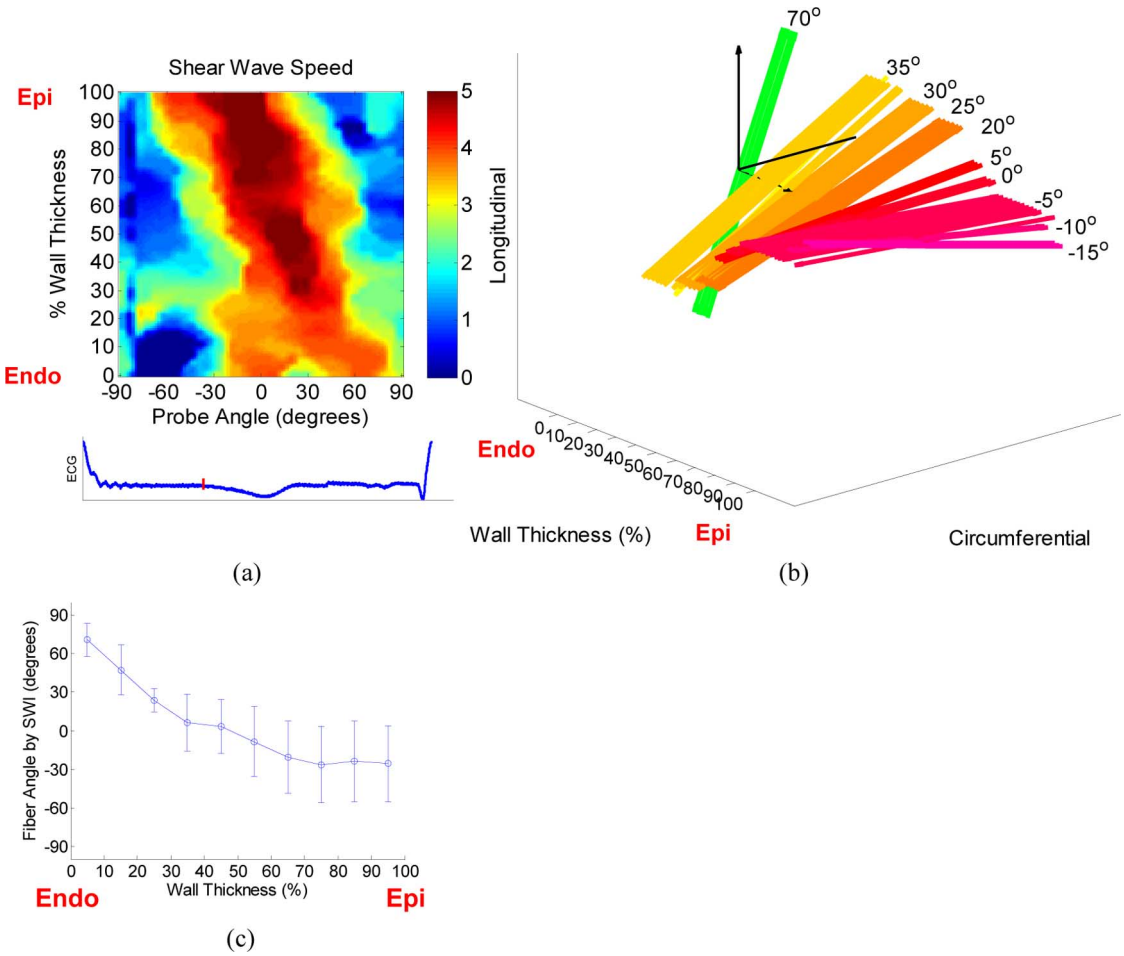


Fig. 7. An example of the shear wave and fiber angle distributions in *in vivo* ovine myocardium at the midsystolic phase. (a) Transmural shear wave speed (displayed on the scale of 0–5 m/s) as a function of the probe angle from one ovine heart; below is the electrocardiogram. (b) Transmural fiber orientation of the same ovine myocardium shown in (a). (c) Average transmural fiber angle orientation estimated by SWI from three ovine myocardia at midsystole *in vivo*. 100% and 0% wall thicknesses represent the epicardium (Epi) and the endocardium (Endo), respectively.

orientation was reconstructed due to the fact that the rotation of the 1-D ultrasound imaging array provided only 1-D overlapped myocardial region, namely, the central axial line of the image data [Fig. 1(b)]. Thirty-seven rotation angles were performed in order to assess 1-D fiber orientation across the myocardial wall (220 samples; 25 mm). The acquisition time for each angle was approximately 6 ms, and the total acquisition time for the complete set of rotation angles required 222 ms. Should a 2-D ultrasound imaging array be available for the SWI technique, 2-D fiber orientation may be reconstructed with SWI with acquisition time favorable for *in vivo* settings.

Our group has previously studied the SWI technique for both time-varying myocardial stiffness over the entire cardiac cycle in open-chest ovine hearts [25] and the correlation between systolic stiffness and the contractility in a Langendorff rat heart model [26]. The knowledge of the myocardial fiber orientation may permit the future investigation of its relationship with myocardial properties as well as deformation during the entire cardiac cycle in both normal and diseased states. The ultimate goal extended from this study is to develop and render SWI as an optional diagnostic tool to simultaneously assess myocardial structure, mechanical properties, and function. Furthermore, the implementation of SWI using the cardiac phased array for noninvasive imaging of myocardial fiber orientation in clinical transthoracic echocardiographic settings is currently under development to examine the effect of attenuation and SNR on fiber mapping accuracy.

## V. Conclusion

In this study, SWI, an echocardiography-based imaging technique, was developed for the assessment of myocardial fiber orientation and has demonstrated its capability of assessing and visualizing myocardial fiber structure in both *in vitro* porcine and *in vivo* ovine hearts. Not only was the transmural variation of the cardiac fiber orientation observed and successfully mapped, but it was also in good qualitative and quantitative agreements with the literature and histology, respectively. Such transmural variation of the myocardial fiber angles was also affirmed by SWI at midsystole in the *in vivo* ovine hearts. The technical infrastructure and the preliminary findings may shed light on the further reconstruction of the fiber orientation using SWI over the entire cardiac cycle in both normal and pathological states, the study of the relationship between the myocardial structure and the dynamics of the myocardial stiffness, the understanding of cardiac remodeling, and the noninvasive visualization of fiber disarray

for the diagnosis of postinfarction remodeling and hypertrophic cardiomyopathy.

## ACKNOWLEDGMENT

The authors would like to thank J. Quillard at Bicêtre Hospital for her assistance in histology scans using optical microscopy and T. Deffieux for helpful discussions.

## REFERENCES

[1] D. D. Streeter and D. L. Bassett, "An engineering analysis of myocardial fiber orientation in pigs left ventricle in systole," *Anat. Rec.*, vol. 155, pp. 503–511, 1966.

[2] D. D. Streeter, H. M. Spotnitz, D. P. Patel, J. Ross, and E. H. Sonnenblick, "Fiber orientation in canine left ventricle during diastole and systole," *Circ. Res.*, vol. 24, pp. 339–347, 1969.

[3] T. Arts, K. D. Costa, J. W. Covell, and A. D. McCulloch, "Relating myocardial laminar architecture to shear strain and muscle fiber orientation," *Am. J. Physiol.-Heart Circul. Physiol.*, vol. 280, pp. H2222–H2229, May 2001.

[4] K. D. Costa, Y. Takayama, A. D. McCulloch, and J. W. Covell, "Laminar fiber architecture and three-dimensional systolic mechanics in canine ventricular myocardium," *Am. J. Physiol.-Heart Circul. Physiol.*, vol. 276, pp. H595–H607, Feb. 1999.

[5] L. K. Waldman, D. Nosan, F. Villarreal, and J. W. Covell, "Relation between transmural deformation and local myofiber direction in canine left-ventricle," *Circ.Res.*, vol. 63, pp. 550–562, Sep. 1988.

[6] D. A. Hooks, M. L. Trew, B. J. Caldwell, G. B. Sands, I. J. LeGrice, and B. H. Smaill, "Laminar arrangement of ventricular myocytes influences electrical behavior of the heart," *Circ. Res.*, vol. 101, pp. E103–E112, Nov. 2007.

[7] A. Kadish, M. Shinnar, E. N. Moore, J. H. Levine, C. W. Balke, and J. F. Spear, "Interaction of fiber orientation and direction of impulse propagation with anatomic barriers in anisotropic canine myocardium," *Circulation*, vol. 78, pp. 1478–1494, Dec. 1988.

[8] D. E. Roberts, L. T. Hersh, and A. M. Scher, "Influence of cardiac fiber orientation on wavefront voltage, conduction-velocity and tissue resistivity in the dog," *Circ. Res.*, vol. 44, pp. 701–712, 1979.

[9] B. Taccardi, E. Macchi, R. L. Lux, P. R. Ershler, S. Spaggiari, S. Baruffi, and Y. Vyhmeister, "Effect of myocardial fiber direction on epicardial potentials," *Circulation*, vol. 90, pp. 3076–3090, Dec. 1994.

[10] C. P. Fleming, C. B. M. Ripplinger, B. Webb, I. R. Efimov, and A. M. Rollins, "Quantification of cardiac fiber orientation using optical coherence tomography," *J. Biomed. Opt.*, vol. 13, pp. 030505-1–030505-5, May-Jun. 2008.

[11] H. Huang, C. MacGillivray, H. S. Kwon, J. Lammerding, J. Robbins, R. T. Lee, and P. So, "Three-dimensional cardiac architecture determined by two-photon microtomy," *J. Biomed. Opt.*, vol. 14, pp. 044029-1–044029-10, Jul.–Aug. 2009.

[12] E. W. Hsu, A. L. Muzikant, S. A. Matulevicius, R. C. Penland, and C. S. Henriquez, "Magnetic resonance myocardial fiber-orientation mapping with direct histological correlation," *Am. J. Physiol.-Heart Circul. Physiol.*, vol. 274, pp. H1627–H1634, May 1998.

[13] D. F. Scollan, A. Holmes, R. Winslow, and J. Forder, "Histological validation of myocardial microstructure obtained from diffusion tensor magnetic resonance imaging," *Am. J. Physiol.-Heart Circul. Physiol.*, vol. 275, pp. H2308–H2318, Dec. 1998.

[14] T. G. Reese, R. M. Weisskoff, R. N. Smith, B. R. Rosen, R. E. Dinsmore, and V. J. Wedeen, "Imaging myocardial fiber architecture in-vivo with magnetic-resonance," *Magn. Reson. Med.*, vol. 34, pp. 786–791, Dec. 1995.

[15] W. Y. I. Tseng, J. G. Dou, T. G. Reese, and V. J. Wedeen, "Imaging myocardial fiber disarray and intramural strain hypokinesis in hypertrophic cardiomyopathy with MRI," *J. Magn. Reson. Imag.*, vol. 23, pp. 1–8, Jan. 2006.

[16] M. T. Wu, W. Y. I. Tseng, M. Y. M. Su, C. P. Liu, K. R. Chiou, V. J. Wedeen, T. G. Reese, and C. F. Yang, "Diffusion tensor magnetic resonance imaging mapping the fiber architecture remodeling in human myocardium after infarction—Correlation with viability and wall motion," *Circulation*, vol. 114, pp. 1036–1045, Sep. 2006.

[17] J. G. Mottley and J. G. Miller, "Anisotropy of the ultrasonic backscatter of myocardial tissue.1. Theory and measurements in vitro," *J. Acoust. Soc. Am.*, vol. 83, pp. 755–761, Feb. 1988.

[18] S. L. Baldwin, K. R. Marutyan, M. Yang, K. D. Wallace, M. R. Holland, and J. G. Miller, "Measurements of the anisotropy of ultrasonic attenuation in freshly excised myocardium," *J. Acoust. Soc. Am.*, vol. 119, pp. 3130–3139, May 2006.

[19] J. Crosby, T. Hergum, E. W. Remme, and H. Torp, "The effect of including myocardial anisotropy in simulated ultrasound images of the heart," *IEEE Trans. Ultrason. Ferroelectr. Freq. Control*, vol. 56, no. 2, pp. 326–333, Feb. 2009.

[20] E. I. Madaras, J. Perez, B. E. Sobel, J. G. Mottley, and J. G. Miller, "Anisotropy of the ultrasonic backscatter of myocardial tissue .2. Measurements in vivo," *J. Acoust. Soc. Am.*, vol. 83, pp. 762–769, Feb. 1988.

[21] M. R. Holland, A. Kovacs, S. H. Posdamer, K. D. Wallace, and J. G. Miller, "Anisotropy of apparent backscatter in the short-axis view of mouse hearts," *Ultrasound Med. Biol.*, vol. 31, pp. 1623–1629, Dec. 2005.

[22] S. A. Wickline, E. D. Verdonk, and J. G. Miller, "3-dimensional characterization of human ventricular myofiber architecture by ultrasonic backscatter," *J. Clin. Invest.*, vol. 88, pp. 438–446, Aug. 1991.

[23] J. Bercoff, M. Tanter, and M. Fink, "Supersonic shear imaging: A new technique for soft tissue elasticity mapping," *IEEE Trans. Ultrason. Ferroelectr. Freq. Control*, vol. 51, no. 4, pp. 396–409, Apr. 2004.

[24] J. L. Gennisson, T. Deffieux, E. Mace, G. Montaldo, M. Fink, and M. Tanter, "Viscoelastic and anisotropic mechanical properties of in vivo muscle tissue assessed by supersonic shear imaging," *Ultrasound Med. Biol.*, vol. 36, pp. 789–801, May 2010.

[25] M. Couade, M. Pernot, E. Messas, A. Bel, M. Ba, A. Hagege, M. Fink, and M. Tanter, "In vivo quantitative mapping of myocardial stiffening and transmural anisotropy during the cardiac cycle," *IEEE Trans. Med. Imag.*, vol. 30, no. 2, pp. 295–305, Feb. 2011.

[26] M. Pernot, M. Couade, P. Mateo, B. Crozatier, R. Fischmeister, and M. Tanter, "Real-time assessment of myocardial contractility using shear wave imaging," *J. Am. Coll. Cardiol.*, vol. 58, pp. 65–72, Jun. 2011.

[27] S. J. Hsu, M. L. Palermi, K. R. Nightingale, S. A. McAleavey, J. D. Dahl, and G. E. Trahey, D. E. Yuhas and S. C. Schneider, Eds., "Shear wave anisotropy imaging," in *Proc. 2003 IEEE Ultrason. Symp. Proc.*, New York, 2003, vol. 1 and 2, pp. 1090–1093.

[28] D. Royer and D. Dieulesaint, *Elastic Waves in Solids I: Free and Guided Propagation*. Berlin, Germany: Springer-Verlag, 2000.

[29] G. Montaldo, M. Tanter, J. Bercoff, N. Benech, and M. Fink, "Coherent plane-wave compounding for very high frame rate ultrasonography and transient elastography," *IEEE Trans. Ultrason. Ferroelectr. Freq. Control*, vol. 56, no. 3, pp. 489–506, Mar. 2009.

[30] P. G. M. de Jong, T. Arts, A. P. G. Hoeks, and R. S. Reneman, "Determination of tissue motion velocity by correlation interpolation of pulsed ultrasonic echo signals," *Ultrason. Imag.*, vol. 12, pp. 84–98, Apr. 1990.

[31] R. O. Duda and P. E. Hart, "Use of hough transformation to detect lines and curves in pictures," *Commun. ACM*, vol. 15, pp. 11–15, 1972.

[32] D. D. Streeter and W. T. Hanna, "Engineering mechanics for succesive states in canine left ventricular myocardium. 2. Fiber angle and sarcomere length," *Circ. Res.*, vol. 33, pp. 656–664, 1973.

[33] Y. Jiang, J. M. Guccione, M. B. Ratcliffe, and E. W. Hsu, "Transmural heterogeneity of diffusion anisotropy in the sheep myocardium characterized by MR diffusion tensor imaging," *Am. J. Physiol.-Heart Circul. Physiol.*, vol. 293, pp. H2377–H2384, Oct. 2007.